A meshless numerical solution of thermo-mechanics of hot-rolled steel bars on a cooling bed

VUGA Gašper[1,a], MAVRIČ Boštjan[1,2,b], HANOGLU Umut[1,3,c] and ŠARLER Božidar[1,3,d] *

[1]Faculty of Mechanical Engineering, University of Ljubljana, Slovenia

[2]Department of Information Technology, Uppsala University, Sweden

[3]Institute of Metals and Technology, Ljubljana, Slovenia

[a]gasper.vuga@fs.uni-lj.si, [b]bostjan.mavric@it.uu.se, [c]umut.hanoglu@imt.si, [d]bozidar.sarler@fs.uni-lj.si

Keywords: Cooling Bed, Steel Bars, Thermo-Mechanics, Strong Form Meshless Method

Abstract. After the continuous hot-rolling process, steel bars are immediately placed on the cooling bed. At the beginning of the cooling, the material is at high temperatures, and the yield strength is low. Due to thermal load, yield strength can be exceeded, and permanent plastic strains start accumulating, resulting in possible unwanted shape changes and residual stresses. The present paper aims to develop a thermo-mechanical model for studying and eliminating undesirable phenomena before the products leave the cooling bed. The governing equations are solved for the two-dimensional slice in a strong form, and a modified version of the radial basis function generated finite difference (RBF-FD) method [1]. The initial bar geometry is obtained from the existing meshless hot-rolling simulation system [2]. The thermal and mechanical models are one-way coupled, i.e. the temperature solution represents a driving force for the stress and strain solution. The temperature field is obtained with explicit propagation in time. The convective and radiative heat fluxes on the boundary are updated at each time step using the ray tracing procedure to determine the radiative heat flux. The mechanical part is solved by considering the small strain elasto-plasticity, where the isotropic von Mises temperature-dependent hardening is employed. The global system of nonlinear equations of the mechanical part is solved by the Newton-Raphson method. The closest point projection method is used to solve the constitutive relations. A sensitivity study is performed on the influence of cooling intensity on a rectangular steel bar's temperature, stress and strain field. We defined the most influential factors for defect formation. For the first time, a novel meshless RBF-FD method is successfully used for solving such a complex industrial problem. The model will be perspectively upgraded from the slice to the three-dimensional model to enable also bending.

Introduction

The meshless strong form radial basis function generated finite difference (RBF-FD) method has gained popularity in modelling different steel production processes. It has been successfully applied to solve large spectra of continuous casting problems, such as diffusion-convection with phase change [1], natural convection influenced by magnetic stirring [3], turbulence phenomena [4], 2D microsegregation with grain growth [5], and 2D thermo-mechanics [6]. Also, multi-pass hot-rolling has been successfully modelled with RBF-FD [2,7], including the grain size prediction [8].

This work represents the first use of RBF-FD for solving the thermo-mechanical response of the last stage of hot-rolling, where the hot-rolled steel bars are cooled. Previous attempts at modelling this step were performed in 1D [9], 2D [10,11] and 3D [12,13]. In [9], the friction with the supports was investigated. In [12], a simple thermo-elastic description has been used and later

extended in [13], including contact with the supports and gravitational load. In [10], the bending of the bars and the residual stresses were computed, and in [11], the flow of surrounding air was included to better predict heat transfer at the boundary. All of the above studies were performed for symmetric and asymmetric rail profiles where the geometry significantly impacts the bending and residual stress formation.

An example of round steel bars cooling on the cooling bed (CB) is shown in Fig. 1 left. A cross-section scheme with rectangular bars (80×39 mm) used in this work is presented in Fig. 1 right. The heat shield with the length of p_l is positioned on top of the CB, raised by p_y from the lowest point of the CB. Each bar starts from the left at the position p_1. After a time t_p, the bar is moved for a distance x_{bp} to the position p_2, and a new bar occupies the position p_1. This movement is repeated until the final position p_n is reached, where the bars leave CB.

The influence of the position of the heat shield above the bars p_y and the distance between the bars x_{bp} on the thermo-mechanical response is investigated.
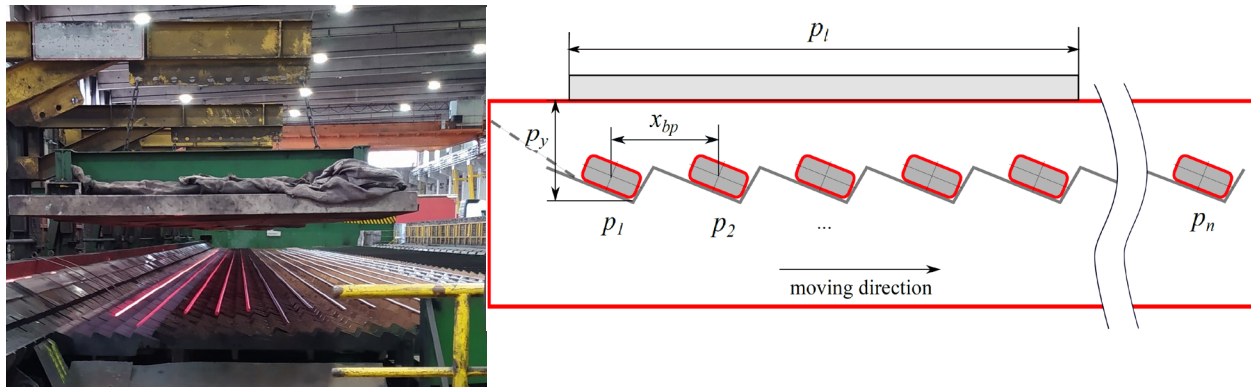

Fig. 1. Left: Photo of the cooling bed. Right: cross-section of the cooling bed with rectangle steel bars present on each position p_i.

Thermal Model
Cooling of the steel bars is governed by the heat diffusion equation

$$\frac{\partial}{\partial t}(\rho c_p T) = \nabla k \cdot \nabla T + k \nabla^2 T \tag{1}$$

where ρ, c_p, k and T stand for the density, the specific heat at constant pressure, the heat conductivity and the temperature, respectively. Material parameters ρ, c_p and k are temperature-dependent. Neumann boundary condition is employed as

$$\mathbf{q} \cdot \mathbf{n} = -k\frac{\partial T}{\partial \mathbf{n}} = q_{conv} + q_{rad} \tag{2}$$

where $\mathbf{q}$ represents the total heat flux and $\mathbf{n}$ is normal at the boundary. The prescribed value on the right-hand side is composed of convective q_{conv} and radiative q_{rad} terms, defined as

$$q_{conv} = h(T - T_{amb}), \qquad q_{rad} = \varepsilon\sigma(T^4 - T_{amb}^{\ 4}) \tag{3}$$

where h, T_{amb}, ε and σ stand for the heat transfer coefficient, the ambient temperature, the emissivity coefficient, and the Stefan-Boltzmann constant, respectively. Since the bars are positioned close to each other, and a heat shield is present above the cooling bed, information about the geometry and the positioning is effectively introduced in q_{rad}. The boundary of the system, composed of the bars and heat shield, is discretized and enclosed inside another discretized closed-loop virtual boundary. The net radiative heat flux of the i-th discretized boundary surface $q_{rad,i}$ is defined as a difference between the emitted heat flux from the surface and the received heat flux from the surroundings as

$$q_{rad,i} = \varepsilon_i \sigma T_i^4 - \sum_{j=1}^{J} \varepsilon_j \sigma T_j^4 \frac{A_j}{A_i} F_{j \to i} \tag{4}$$

where the received part is defined as a sum over all J discrete surfaces (DSs). DS visibility is defined by the view factor $F_{j \to i} \in [0,1]$. It represents the portion of the radiation emitted by the surface A_j received by the surface A_i [14].

Mechanical Model
This work considers small strain elasto-plasticity with von Mises flow rule and isotropic hardening. The mechanical equilibrium of the steel bar is described by the balance law

$$\nabla \cdot \boldsymbol{\sigma} = \mathbf{f} \tag{5}$$

where $\boldsymbol{\sigma}$ is the stress tensor and $\mathfrak{f}$ is the body force. The strain tensor is defined in terms of displacement $\mathbf{u}$ as $\boldsymbol{\varepsilon} = 1/2(\nabla \mathbf{u} + \nabla \mathbf{u}^\top) = \nabla^s \mathbf{u}$. It can be split into elastic $\boldsymbol{\varepsilon}^e$ and plastic $\boldsymbol{\varepsilon}^p$ terms $\boldsymbol{\varepsilon} = \boldsymbol{\varepsilon}^e + \boldsymbol{\varepsilon}^p$. The relationship between stresses and strains is defined by the Hooke's law

$$\boldsymbol{\sigma} = \mathsf{D}^e \boldsymbol{\varepsilon}^e = \mathsf{D}^e(\boldsymbol{\varepsilon} - \boldsymbol{\varepsilon}^p) \tag{6}$$

where D^e represents the fourth-order elasticity tensor. The employed von Mises yield criterion states that the material yields when von Mises stress $\sigma_{vm} = \sqrt{3J_2}$ exceeds the yield stress obtained from the uniaxial tensile test σ_y. J_2 represents the second invariant of the deviatoric part $\mathbf{s} = \boldsymbol{\sigma} - \mathbf{I}\,\mathrm{tr}(\boldsymbol{\sigma})/3$ of the stress tensor, where $\mathbf{I}$ is the identity tensor. The evolution of the yield stress is defined by a hardening law $\sigma_y = \sigma_y(\overline{\varepsilon}^p, T)$, assumed to be a nonlinear function of the temperature and the accumulated plastic strain $\overline{\varepsilon}^p = \sqrt{2/3}\,\|\boldsymbol{\varepsilon}^p\|$. Johnson-Cook strain rate independent hardening law is used

$$\sigma_y(\overline{\varepsilon}^p, T) = \left(A + B\left(\overline{\varepsilon}^p\right)^n\right)\left(1 - \left(\frac{T - T_0}{T_m - T_0}\right)^m\right) \tag{7}$$

where all constants are determined by fitting 46MnVS5 steel data obtained by the JMatPro software. Admissible stress states are compactly specified with a yield function

$$\Phi(\boldsymbol{\sigma}, \sigma_y) = \sqrt{3 J_2(\mathbf{s}(\boldsymbol{\sigma}))} - \sigma_y \le 0 \tag{8}$$

where $\Phi(\boldsymbol{\sigma}, \sigma_y) < 0$ holds in the elastic regime and $\Phi(\boldsymbol{\sigma}, \sigma_y) = 0$ holds in the plastic regime. The evolution of the plastic strain is defined in the rate form by a plastic flow rule

$$\dot{\boldsymbol{\varepsilon}}^p = \dot{\gamma} \frac{\partial \Phi}{\partial \boldsymbol{\sigma}} = \dot{\gamma} \sqrt{\frac{3}{2}} \frac{\mathbf{s}}{\|\mathbf{s}\|} \tag{9}$$

where γ represents the plastic multiplier and connects the strain and the stress space. Lastly, a set of loading/unloading conditions is given as

$$\Phi(\boldsymbol{\sigma}, \sigma_y) \le 0, \quad \dot{\gamma} > 0, \quad \Phi(\boldsymbol{\sigma}, \sigma_y)\dot{\gamma} = 0 \tag{10}$$

that have to be fulfilled. Since the material response is path-dependent, Eq. 5 is solved incrementally. For a $(n+1)$-th load increment, it can be written in the form $\mathbf{f}^{\text{int}}\big|_{n+1} - \mathbf{f}^{\text{ex}}\big|_{n+1} = \mathbf{r}(\mathbf{u}_{n+1}) = 0$, where $\mathbf{r}$ represents the residual that should be zero, $\mathbf{f}^{\text{ex}}$ external load, and $\mathbf{f}^{\text{int}}$ internal force defined as $\mathbf{f}^{\text{int}} = \nabla \cdot \boldsymbol{\sigma}(\nabla^s \mathbf{u})$. Due to a nonlinear relationship between stress and strain, the residual is linearized as

$$\nabla \cdot \left(\mathsf{D}\nabla^s\right)\Big|_{n+1}^k \delta\mathbf{u} = -\mathbf{r}\big|_{n+1}^k \tag{11}$$

where $\mathsf{D} = \partial\boldsymbol{\sigma}/\partial\boldsymbol{\varepsilon}$. Eq. 11 is iteratively (index k) solved for $\delta\mathbf{u}$. After each k-th iteration, the displacement increment is updated as $\Delta\mathbf{u}^k = \Delta\mathbf{u}^{k-1} + \delta\mathbf{u}$. From here, the strain increment $\Delta\boldsymbol{\varepsilon}^k$ is determined and inserted into the integration model, where all other state variables are updated, solving Eqs. 6-10. When $\delta\mathbf{u}$ is sufficiently small, the displacement is updated as $\mathbf{u}_{n+1} = \mathbf{u}_n + \Delta\mathbf{u}$. Since only temperature load is applied on the steel bars, the external load is defined as $\mathbf{f}^{\text{ex}}_{n+1} = \nabla \cdot ((3\lambda + 2G)\alpha\Delta T\mathbf{I})\big|_{n+1}$, where λ, G, α and ΔT stand for the first and the second Lamé's constants, the linear expansion coefficient, and the temperature difference ($\Delta T = T_{n+1} - T_n$), respectively. Between bars and the cooling bed, no contact is assumed. The Neumann type of boundary condition is prescribed on the whole boundary $\mathbf{t} = \boldsymbol{\sigma} \cdot \mathbf{n} = 0\,\text{N/m}$, where $\mathbf{t}$ represents the traction vector. Since only the derivatives of the displacement field are defined, two additional conditions are enforced to obtain a unique solution

$$\int_{\Omega} \mathbf{u}(\mathbf{r})d\Omega = 0 \quad , \quad \int_{\Omega} \left(\mathbf{u}(\mathbf{r}) \times \mathbf{r}\right)d\Omega = 0 \tag{12}$$

where Ω represents the bar cross-section area, and $\mathbf{r}$ is a position vector. The posed equations are solved within a plane strain assumption.

Numerical Method

Spatial discretization is performed using the RBF-FD method. The observed domain is discretized by a homogeneous distribution of the scattered discretization nodes - collocation nodes (CNs). For each CN, a set of closest local neighbours is determined that constructs the so-called local

subdomains $_l\Omega, l \in [1, N_{all}]$, where N_{all} represents the number of all CNs. Inside each $_l\Omega$, the interpolation of a general function can be written as

$$_l y_\xi(\mathbf{r}) \approx \sum_{i=1}^{_lN} {}_l\alpha_{i,\xi} \, {}_l\Phi_i(\mathbf{r}) + \sum_{i=1}^{M} {}_l\alpha_{(_lN+i),\xi} \, p_i(\mathbf{r}) = \sum_{i=1}^{_lN+M} {}_l\alpha_{i,\xi} \, {}_l\Psi_i(\mathbf{r}) \tag{13}$$

where ξ is the index that runs over space dimensions n_d, $_lN$ is the number of CNs inside $_l\Omega$ and is here set to $_lN = 13$, $_l\alpha_{i,\xi}$ represents weight coefficients, and $_l\Phi_i(\mathbf{r})$ is the Radial Basis Function (RBF). Various types of RBFs can be used in the RBF-FD method. Here, 3rd order polyharmonic splines [15] (PHSs) are employed as $_l\Phi_i(\mathbf{r}) = (\|\mathbf{r} - {}_l\mathbf{r}_i\| / {}_lh)^3$, where $_lh$ represents the average distance from the centre of $_l\Omega$ to its neighbours inside $_l\Omega$. The interpolant is augmented with monomials $p_i(\mathbf{r}), i \in [1, M]$, where $M = 3$ for the 2nd order augmentation $p_1 = x, p_2 = y, p_3 = 1$ used here. Eq. 13 can be compactly written as a system of $n_d(_lN + M)$ linear equations

$$\sum_{\chi=1}^{n_d} \sum_{i=1}^{_lN+M} {}_lA_{ji,\chi\xi} \, {}_l\alpha_{i,\chi} = {}_l\gamma_{j,\xi}$$

where

$$_lA_{ji,\xi\chi} = \begin{cases} \Psi_i(_l\mathbf{r}_j)\delta_{\xi\chi} & \text{if } _l\mathbf{r}_j \in \Omega \cup \Gamma \\ p_{j-_lN}(_l\mathbf{r}_j)\delta_{\xi\chi} & \text{if } j > {}_lN \text{ and } i \le {}_lN \\ 0 & \text{otherwise} \end{cases} \qquad _l\gamma_{j,\xi} = \begin{cases} y_\xi(_l\mathbf{r}_j) & \text{if } _l\mathbf{r}_j \in \Omega \cup \Gamma \\ 0 & \text{otherwise} \end{cases} \tag{14}$$

Application of a linear differential operator L on the interpolation function Eq. 13 acts only on the basis functions

$$L_l\mathbf{y}(\mathbf{r})_\xi = \sum_{\chi=1}^{n_d} L_{\xi\chi} {}_l y_\chi(\mathbf{r}) \approx \sum_{\chi=1}^{n_d} \sum_{i=1}^{_lN+M} {}_l\alpha_{i,\chi} L_{\xi\chi} {}_l\Psi_i(\mathbf{r}) \tag{15}$$

Expressing weight coefficients from Eq. 14, we arrive at

$$L_l\mathbf{y}(\mathbf{r})_\xi \approx \sum_{\zeta=1}^{n_d} \sum_{j=1}^{_lN+M} {}_l\gamma_{j,\zeta} \sum_{\chi=1}^{n_d} \sum_{i=1}^{_lN+M} {}_lA_{ij,\chi\zeta}^{-1} L_{\xi\chi} {}_l\Psi_i(\mathbf{r}) = \sum_{\zeta=1}^{n_d} \sum_{j=1}^{_lN+M} {}_l\gamma_{j,\zeta} \, {}_lW_{j,\xi\zeta}(\mathbf{r}) \tag{16}$$

where the operator's action on a function is now expressed as a weighted sum of known values $_l\gamma_{j,\zeta}$ and operator coefficients $_lW_{j,\xi\zeta}(\mathbf{r})$. So, in order to discretize differential operators, the operator coefficients (OCs) should be determined for each $_l\Omega$. This is done as a pre-prosses step only once.

Regarding the governing equation of the thermal model Eq. 1, OCs for the gradient and the Laplacian operator of the scalar field are computed. Time marching is performed with the forward Euler method. View factor matrix $\mathbf{F}$, which includes the view factor $F_{j \to i}$ for each (j, i) DS pair,

is computed with the Monte Carlo method. Here $N_{vf} = 10^5$ particles are shoot in random directions from j-th DS and checked which i-th DS is hit. Based on the number of hit particles in the i-th DS the $F_{j \to i}$ component is determined. In case DS is reflective, the $N_{vf} \cdot \zeta$ number of random particles is bounced off, where ζ is the reflection coefficient.

Discretization of the differential operators in the governing equation Eq. 11 of the mechanical model is performed slightly differently than in the thermal model for increasing stability. OCs of ∇^s operator are not evaluated in CNs but on the 2nd order finite difference (FD) stencils prescribed separately to each CN when CN lies inside the domain. Then, the divergence operator is evaluated via the FD method. The distance between CN and its nearest point on the FD stencil equals $h/2$, where h is the distance to the nearest CN. On the boundary, where only OCs of ∇^s are needed, the position of evaluation of COs is moved for $h/2$ in the opposite side of the outward-facing normal vectors. With the OCs computed, a sparse global system of equations is assembled and solved to obtain the solution. Our future work will publish a more detailed description of the procedure.

Simulation Procedure

The thermal simulation starts by importing the bar's discretized domain (CNs), placing it on the first stage p_1, and setting the material parameters based on the initial temperature $T_{bar,0}$. For the determination of radiative heat fluxes, the CB is enclosed inside the virtual rectangle shown with the red contour in Fig. 1. The boundary of the first bar (also shown with the red contour in Fig. 1) is discretized on DSs. Then, the view factor matrix **F** is computed with DSs of the rectangle and the first bar. Three types of DSs are considered: the first one belongs to the heat shield with reflectivity ζ_{pl}, the second to the steel bars with reflectivity ζ_{bar}, and the third to all other surfaces with reflectivity ζ_{sur}. The heat shield temperature and ambient temperature are set to T_{pl} and T_{sur}, respectively. With **F** computed, heat fluxes on the boundary are calculated using the remaining parameters shown in Table 1. The simulation runs until t_p is reached, where during time marching, the heat fluxes on the boundary and material parameters are updated before each time step. After that, the bar is moved to p_2, and a new bar is positioned on p_1. Since 2 bars are now included, a new **F** is computed. The simulation runs again until t_p where 2 bars are now cooled. This process is repeated with 3, 4, and so on bars until the last position p_n is reached. Then a new cycle is run where the bar on p_n position is removed from the system. Adding the bars on the CB (from the left side) and removing them (from the right side) is repeated until the temperature difference at the time t_p in the centre of the bar on the last stage p_n between two cycles is less than ΔT_{max}. With this procedure, the quasi-steady state temperature solution is obtained.

The temperature solution is position (or stage) dependent $T(\mathbf{r}, t_j, p_i), t_j \in [0, t_p]$. For mechanical simulation, it is transformed to $T(\mathbf{r}, t_j), t_j \in [0, t_p \, p_n]$ since an arbitrary bar can be picked for the analysis. The mechanical model then incrementally applies the temperature load and considers the updating of the material parameters.

In this work, we show the influence of the distance between bars x_{bp} and the position of the heat shield p_y on the thermal and mechanical solution fields. The study is performed for three different x_{bp}s (R1, R2, R3). To study the same time window $t_{max} = t_p \cdot p_n$, different times on each stage t_p and a different number of maximum stages p_n are applied. Also, three different p_ys (P1, P2, P3) are investigated, as shown in Table 2.

Table 1. Constants used in the thermal model.

$\varepsilon_{pl}, \varepsilon_{bar}, \varepsilon_{sur} [/]$		$\zeta_{pl}, \zeta_{bar} [/]$	$\zeta_{sur} [/]$	$T_{pl} [°C]$	$T_{bar,0} [°C]$	$T_{sur} [°C]$	$h [W/m^2K]$	$\Delta T_{max} [°C]$
0.8		0.2	0	300	900	25	20	0.5

Table 2. Parameters used in the case studies.

	x_{bp} [m]	t_p [s]	p_n [/]		p_y [m]
R1	0.15	5	30	P1	0.3
R2	0.3	10	15	P2	0.7
R3	0.45	15	10	P3	1.3

Results of the Thermal Model

In Fig. 2, the temperature solution in the centre of the bar for the P1R1 case (T_{P1R1}) and the difference to other cases $T_{diff} = T_{P1R1} - T_{PiRi}$ are shown over time. In the P1R1 case, the bars are close to each other, and the heat shield is at its lowest point. Due to that, the slowest cooling is obtained. In all cases, the temperature sensitivity to the position of the heat shield is small. With a larger p_y, the bar's centre is additionally cooled for ~1°C. A comparison of R1 and R2 shows that x_{bp} has a more significant impact on the solution than p_y. In the end, the centre point is cooled for ~5°C more. In case of increased spacing between the bars (compare R2 and R3), the temperature drop is much lower ~1°C.
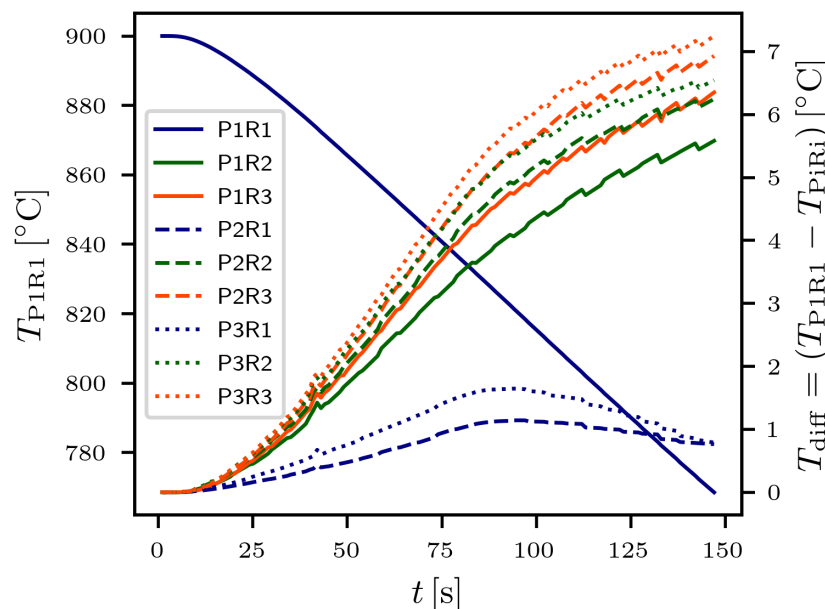

Fig. 2. P1R1 temperature solution in time at the centre of the bar and the difference to other cases.

Fig. 3 shows the temperature solution at the end of the simulation over the field for all investigated cases. As shown before, observing cases from left to right (increasing x_{bp}), the temperature decreases more than changing the cases from top to bottom (increasing p_y). One can also observe that the field is not symmetric. This is a consequence of nonuniform heat fluxes that change with time. In all cases, the right half of the bar is cooled more. This happens since a bar on the right-hand side of some other observed bar is colder than the bar on the left-hand side, so the heat flux on the right is larger.
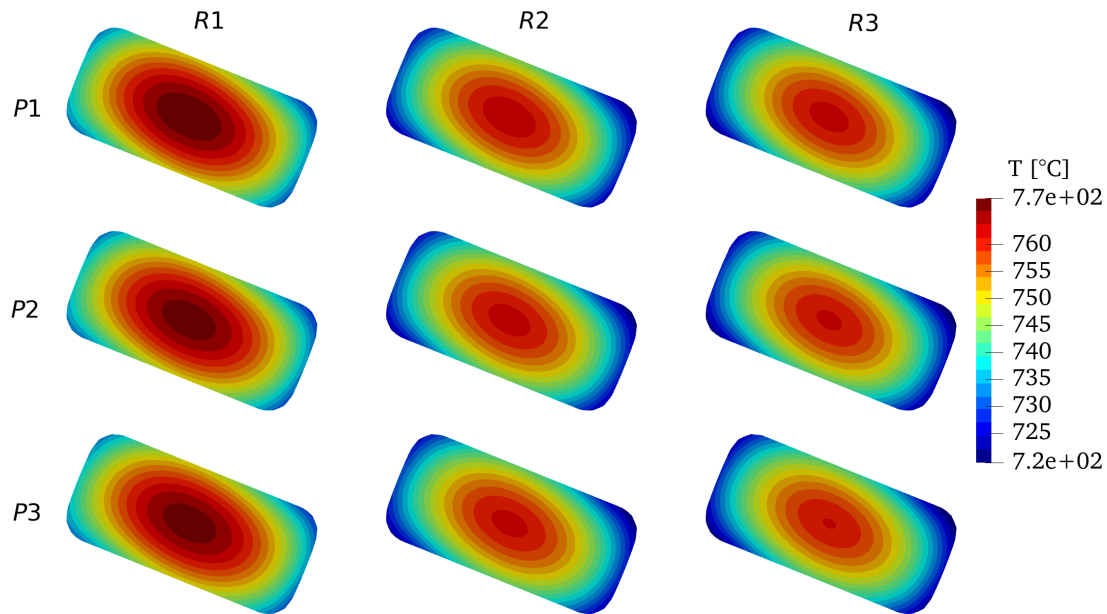
Fig. 3. Temperature of all cases as a function of x_{bp} and p_y at $t_{max} = 150$ s.

Results of the Mechanical Model

In Fig. 4, the results of the von Mises stress σ_{vm} and the accumulated plastic strain $\bar{\varepsilon}^p$ are shown over time obtained in the centre point of the bar. Up to $t \approx 5$ s, the elastic response occurs where no plastic strain is present. Then the slope of the σ_{vm} changes and the bar is plastically deformed. One can see that σ_{vm} and $\bar{\varepsilon}^p$ are changing mostly linearly with time. Small differences in solutions at the end of the simulation are obtained. As in the temperature solution, cases with the same x_{bp} have a similar solution.
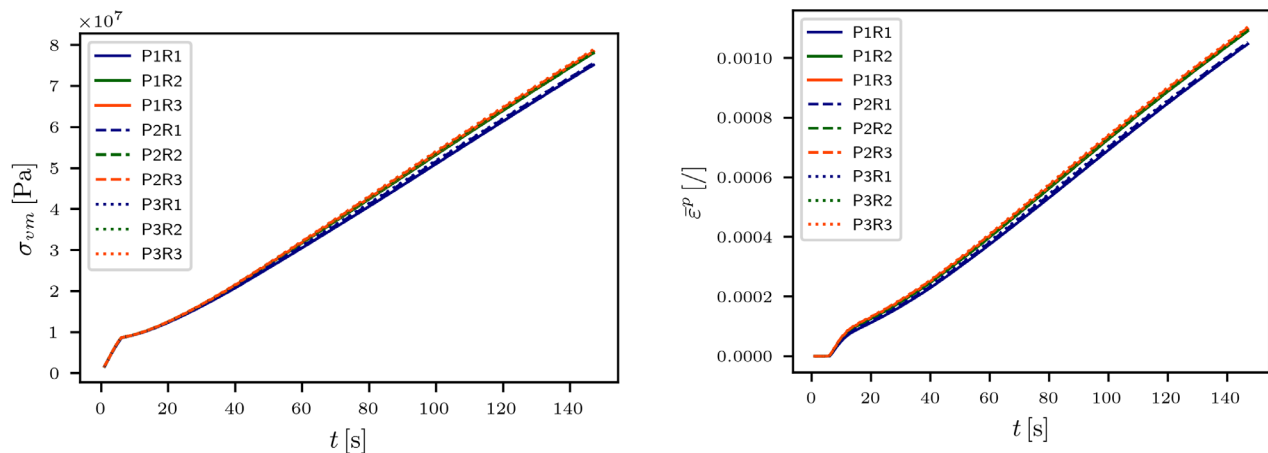

Fig. 4. Von Mises stress (left) and accumulated plastic strain (right) in the centre of the bar over time.

In Fig. 5, the von Mises stress is shown over the field for all cases at the end of the simulation. Similar asymmetry as in the temperature field can be observed. The highest stresses occur in the same area as the lowest temperatures.

In Fig. 6, the initial shape is shown with a grey colour contour. For comparison with deformed shapes, it is shrunk by a factor of 16. The deformed contours, also shown in Fig. 6, are obtained by applying the displacement field solution, multiplied by 300, onto the initial geometry to make

the change visible. In the R1 case, the shrinkage is the smallest, and in the R3 case is the largest. All deformed shapes have a more elliptic shape and are also slightly tilted to the left.
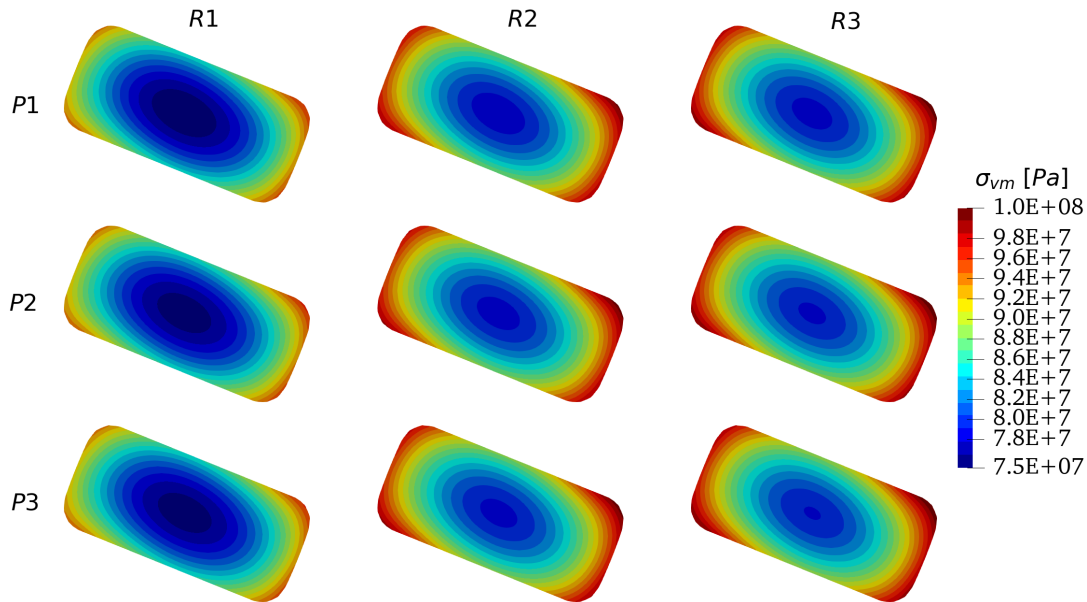

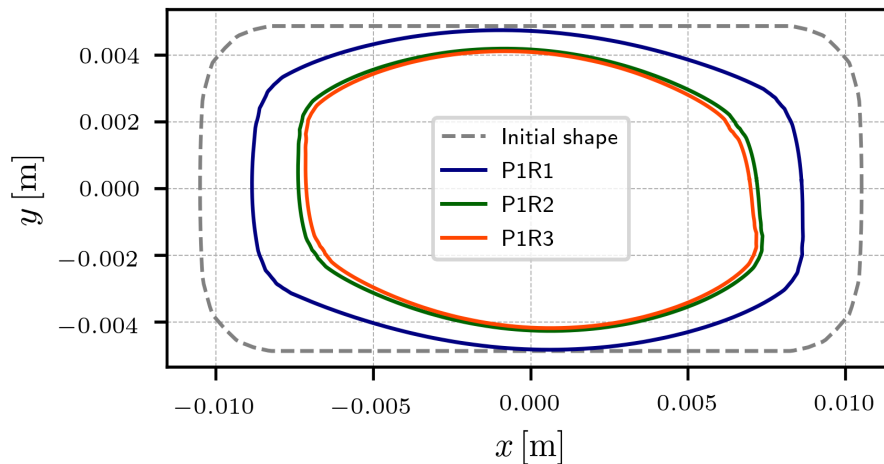Fig. 5. Von Mises stress of all cases as a function of x_{bp} and p_y at $t_{max} = 150$ s.

Fig. 6. Initial shape contour shrank by a factor of 16. Deformed contours are obtained by applying the displacement solution multiplied by a factor 300.

Summary

In this work, we presented the modelling of a thermo-mechanical response of steel bars on the cooling bed with the RBF-FD method. Nine cases with varying distances between bars and the position of the heat shield were investigated. We have shown that the solution fields and the final geometry are not symmetric. A reduction of distance between bars has proven to be much more dominant in reducing the cooling rate than the reduction of spacing between bars and the heat shield. The calculated accumulated plastic strain in all considered cases ranges up to ∼0.1%, and the maximum von Mises stresses obtained are ∼100 MPa.

With this work, we have successfully demonstrated the use of the RBF-FD method on a complex industrial problem. In future work, a three-dimensional model will be implemented to capture also bending of the bars.

Acknowledgements

References

[1] R. Vertnik, B. Šarler, Meshless local radial basis function collocation method for convective-diffusive solid-liquid phase change problems, Int. J. Numer. Meth. Heat Fluid Flow 16 (2006) 617-640. https://doi.org/10.1108/09615530610669148

[2] U. Hanoglu, B. Šarler, Multi-pass hot-rolling simulation using a meshless method, Comput. Struct. 194 (2018) 1-14. https://doi.org/10.1016/j.compstruc.2017.08.012

[3] K. Mramor, R. Vertnik, B. Šarler, Simulation of Natural Convection Influenced by Magnetic Field with Explicit Local Radial Basis Function Collocation Method, CMES - Comput. Model. Eng. Sci. 92 (2013) 327-352.

[4] K. Mramor, R. Vertnik, B. Šarler, Meshless approach to the large-eddy simulation of the continuous casting process, Eng. Anal. Bound. Elem. 138 (2022) 319-338. https://doi.org/10.1016/j.enganabound.2022.03.001

[5] B. Šarler, R. Vertnik, A. Lorbiecka, I. Vušanović, B. Senčič, A multiscale slice model for continuous casting of steel, IOP Conf. Ser. Mater. Sci. Eng. 33 (2012). https://doi.org/10.1088/1757-899X/33/1/012021

[6] B. Mavrič, T. Dobravec, R. Vertnik, B. Šarler, A meshless thermomechanical travelling-slice model of continuous casting of steel, IOP Conf. Ser. Mater. Sci. Eng. 861 (2020) 012018. https://doi.org/10.1088/1757-899x/861/1/012018

[7] U. Hanoglu, B. Šarler, Hot Rolling Simulation System for Steel Based on Advanced Meshless Solution, Metals 9 (2019) 788. https://doi.org/10.3390/met9070788

[8] U. Hanoglu, B. Šarler, Developments towards a Multiscale Meshless Rolling Simulation System, Materials 14 (2021) 4277. https://doi.org/10.3390/ma14154277

[9] L.V. Nikitin, F.D. Fischer, E.R. Oberaigner, F.G. Rammerstorfer, M. Seitzberger, R.I. Mogilevsky, On the frictional behaviour of thermally loaded beams resting on a plane, Int. J. Mech. Sci. 38 (1996) 1219-1229. https://doi.org/10.1016/0020-7403(96)00009

[10] J. Basu, S.L. Srimani, D.S. Gupta, Rail behaviour during cooling after hot rolling, J. Strain Anal. Eng. Des. 39 (2004) 15-24. https://doi.org/10.1177/030932470403900102

[11] A. Pernía-Espinoza, F.J. Ascacibar, E. Martínez-de-Pisón, J. Blanco, Analysis of rail cooling strategies through numerical simulation with instant calculation of thermal expansion coefficient, Rev. Metal. 46 (2010). https://doi.org/10.3989/revmetalm.0911

[12] M. Abouaf, J.-L. Chenot, J.-L. Marcelin, A two-dimensional finite element idealization for thermo-elastic deflection in beams, Int. J. Numer. Methods Eng. 19 (1983) 1453-1465. https://doi.org/10.1002/nme.1620191004

[13] I.I. Boyadjiev, P.F. Thomson, Y.C. Lam, Prediction of the deflection and residual stress in controlled cooling of hot-rolled steel beams including load and arbitrary support: Part I. Computational model, J. Mater. Process. Technol. 147 (2004) 370-376. https://doi.org/10.1016/j.jmatprotec.2004.01.009

[14] A. Jaklič, F. Vode, T. Kolenko, Online simulation model of the slab-reheating process in a pusher-type furnace, Appl. Therm. Eng. 27 (2007) 1105-1114. https://doi.org/10.1016/j.applthermaleng.2006.07.033

[15] G.E. Fasshauer, Meshfree Approximation Methods with Matlab: (With CD-ROM), World Scientific 6 (2007). https://doi.org/10.1142/6437